High-resolution subsurface articular cartilage imaging based on Fourier-domain common-path optical coherence tomography

Jae-Ho Han[1], Xuan Liu[1], Jin U. Kang[1], and Chul Gyu Song[2*]

[1] *Department of Electrical and Computer Engineering, Johns Hopkins University, 3400 N. Charles St., Baltimore, MD 21218, USA*

[2] *Division of Electronics and Information Engineering, Center for Advanced Image and Information Technology, Chonbuk National University, Deokjin-Dong, Jeonju, 561-756, Korea*

[*] *E-mail: song133436@gmail.com*

Received September 17, 2009

We demonstrate the subsurface imaging of an articular cartilage using Fourier-domain common-path optical coherence tomography. The bare fiber probe integrated with a hypodermic needle provides the rigidness required to perform lateral scanning with less microscale bending. By submerging both the probe and the specimen into saline solution, we not only reduce the beam divergence, but also increase the signal-to-noise ratio compared with the measurement in free space. Our system can differentiate the characteristic cartilage zones and identity various micro-structured defects in an *ex vivo* chicken knee cartilage, thus demonstrating that it could be used to conduct early arthritis diagnosis and intraoperative endo-microscopy.

OCIS codes: 110.4500, 170.0110, 030.1670, 060.2310.
doi: 10.3788/COL20100802.0167.

It is crucial for micro-structural degenerative joint disease (DJD) or osteoarthritis in articular cartilage, which has been reported to be the most common cause of chronic physical disability, to be detected and assessed both early and accurately[1]. Due to the use of a broadband near infrared light source, optical coherence tomography (OCT) has unprecedented subsurface resolution compared to the conventional morphological cross-sectional imaging modalities, such as computed tomography (CT), ultrasound and magnetic resonance imaging (MRI) or arthroscopy, which are limited to the assessment of magnified surface lesions[2]. Especially, Fourier-domain (FD) common-path (CP) OCT has gained much attention, due to its inherently high signal-to-noise ratio (SNR), higher speed, and the fact that it is simple and less sensitive to external perturbations such as vibration and temperature[3,4]. Because the same fiber optic path is used for the sample and the reference arms, there is no need to compensate for the mismatches in the dispersion and polarization of the two arms by using a CP configuration. Such a configuration is also attractive for clinical and biomedical applications, in which the diagnostic and surgical probe can be interchangeable with an arbitrary length and disposable with high stability[5]. In addition, a minimally invasive optic probe that can be integrated into a conventional diagnosis catheter and arthroscope is desirable, since it can be inserted directly into various articular cartilages, as demonstrated in *in vivo* proximity and imaging tools, for example in the cases where Chu inserted an OCT probe into an arthroscope[6] and/or Pan made a hand-held OCT probe that guides the arthroscope[7]. Furthermore, Chu *et al.* reported a polarization sensitive OCT device for articular cartilage imaging with a human cadaver[8] and bovine sample[9], thereby enhancing the image results by manipulating the birefringence properties of the tissue; Li *et al.* utilized an OCT system to perform *in vivo* human osteoarthritic cartilage surgery in conjunction with an aiming beam[10]; Youn *et al.* used an OCT probe as a displacement sensor, while measuring the electrokinetic response of the cartilage[11]; and non-invasive optical biopsy after cartilage repair was performed with OCT by Han *et al.*[12] In this letter, we explore the efficacy of Fourier-domain common-path OCT (FD-CPOCT) operating in a shorter near infrared range using a simple 125-μm bare optic fiber probe to obtain higher depth resolution characteristic layers and detailed lesion features in the knee cartilage. This method could be used in various kinds of arthritis for the early and accurate diagnosis and detection of degeneration. We also characterize the SNR, as well as the beam divergence of the probe, in a liquid environment.

A schematic view of the experimental setup for the FD-CPOCT is presented in Fig. 1. The FD-CPOCT system consists of a single super luminescent diode (SLD) employed as a low-coherence broadband light source and a fiber coupler for directing the beam to a fiber-optic probe and redirecting the returned beam to a high resolution spectrometer with a 3648-pixel charge-coupled device (CCD) array. Its spectral data are analyzed or Fourier transformed to extract the depth (distance) information from the intensity modulated optical spectra. We used a center wavelength of 835 nm with a 37-nm bandwidth SLD which has a corresponding coherence length or depth resolution of 8 μm. The 125-μm-diameter bare optic fiber probe was attached to a translational stage or to a galvanometer for lateral (transverse) scanning with a step size of 1 μm. This optic fiber is small enough to be integrated into conventional 20–25 Ga hypodermic needles. To mimic the *in vivo* aqueous condition in the articular cartilage joint, which is originally filled with synovial fluid, we submerged a piece of an *ex vivo* chicken

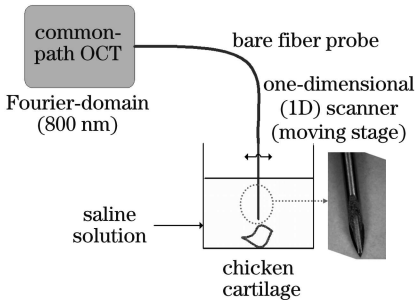

Fig. 1. Experimental setup for the FD-CPOCT system with a single micro-bare fiber probe (inset photo: prototype integrated bare fiber needle probe).

knee cartilage into 0.9% NaCl (saline) solution. Because the fiber end is not coated, by submerging the uncoated bare fiber probe into the saline solution, it experiences a reduced reference signal strength, due to the smaller Fresnel reflection between the fiber probe and saline solution. Instead, to maintain the appropriate level of reference amplitude in the saline solution, we simply increased the power of the launching SLD source, so that the reference signal strength was not reduced and, consequently, the overall SNR was not changed. We inserted a bare fiber with an outer diameter of 0.245 mm and a polymer jacket into a 25-Ga needle with an inner diameter of 0.25 mm and glued the fiber to the inside of a 5-cm-long metallic needle using epoxy. The remaining optical fiber and the upper part of the needle are fixed to the translational stage by mechanical mounts for lateral scanning. By integrating the bare fiber probe into the surgical needle, we can prevent the micro-vibration or bending of the fiber probe while moving the lateral scanner.

In Fig. 2, we characterize the implemented FD-CPOCT system in saline solution. The numerical aperture (NA) of the single mode fiber we used was 0.14 in free space or air ($n_{\rm air} = 1.00$), so that the illuminating beam diverge with an angle of $\pm 8^\circ$. However, in the saline solution with $n_{\rm saline} = 1.34$, the angle is reduced to $\pm 6^\circ$ (a smaller beam spot size), which affects the lateral resolution of the image results, as shown in Fig. 2(a). In the case of a non-focusing beam from an optical fiber, the lateral resolution is not simply a function of the beam divergence, but also the dimension of the coupling single mode fiber. We achieved axial and lateral resolutions of 8 and 5 μm, respectively, at a distance of approximately 100 μm.

Notably, submerging the sample in saline solution helps to decrease the surface reflection from the sample and accordingly increases the amount of power detected from the inside of the sample, thus increasing the SNR. The SNR can be written as[13]

$$\mathrm{SNR} = 10\lg\left(\frac{\gamma}{\left(\frac{(\gamma+1)}{N_{\rm s}} + \frac{N}{2\tau\Delta v_{\rm eff}}(\gamma+1)^2 + \frac{1}{N_{\rm s}^2}\left(\sigma_{\rm dark}^2 + \sigma_{\rm read}^2\right)\right)\frac{1}{N}}\right), \tag{1}$$

where γ is the ratio between the reference power $P_{\rm r}$ and sample power $P_{\rm s}$; $\Delta v_{\rm eff}$ is the effective spectral line width[14]; N is the number of CCD pixels; τ is the CCD exposure time; $N_{\rm s}$ is proportional to the sample power as $N_{\rm s} = \left(\frac{S\eta\tau P_{\rm s}}{Nh\nu_0}\right)$ and h is Planck's constant; $\sigma_{\rm dark}^2$ is the dark noise of the detector and $\sigma_{\rm read}^2$ is the read noise. In our system, the dark noise is about 8 counts and the read noise is about 50 counts. From Eq. (1), one can see that the SNR depends on the power reflected back from the sample, as well as the reference to sample power ratio γ. However, γ and $N_{\rm s}$ are not independent of each other, because, practically, the CCD is operating near the saturation regime. In other words, the total number (S) of photons that can be detected in one pixel cannot be larger than the limitation (S_0) set by the quantum well of the CCD. The interference spectrum (s) can be expressed as

$$s = \frac{S\eta\tau}{h\nu_0}\left[P_{\rm r} + P_{\rm s} + 2\sqrt{P_{\rm r}P_{\rm s}}\cos(4\pi kl)\right], \tag{2}$$

where η is the detector quantum efficiency and ν_0 is the center frequency of the light source spectrum. Especially, in the case of $\cos(4\pi kl) = 1$, the interference spectrum reaches the maximum as

$$s_{\max} = N_{\rm s}\left(1 + \sqrt{\gamma}\right)^2 = S_0. \tag{3}$$

Therefore, this results in

$$N_{\rm s} = S_0/\left(1 + \sqrt{\gamma}\right)^2. \tag{4}$$

Using Eqs. (1) and (4), we obtain Fig. 2(b) showing the relationship between γ and SNR. It is shown that the maximum SNR is obtained when the reference power is almost equal to the sample power. Most of the power from the source will be incident onto the sample; because the reflection at the fiber end is small (∼0.2%) and the sample power is almost constant, no matter what medium is present between the fiber end and the sample. However, the reference power changes prominently when the probe is in the saline solution. Moreover, the sample power is usually much smaller than the reference power and, hence, the system operates in the left-most part of the curve. Therefore, the larger the ratio γ (indicating a smaller reference power) becomes, the better the SNR that we are going to achieve. We can also achieve a better imaging depth, due to the lesser reflection between the saline solution and tissue interface and the increase in the penetrating beam power, as well as the smaller diverging angle. Additionally, the matched index results in a better returned sample power coupling to the fiber

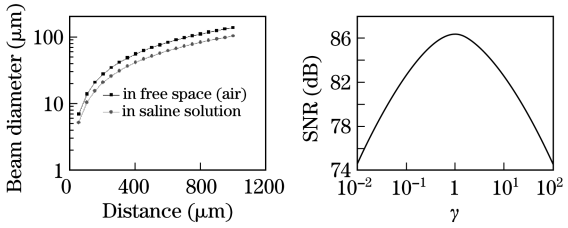

Fig. 2. Characteristics of the system: (a) probing beam divergence; (b) SNR.

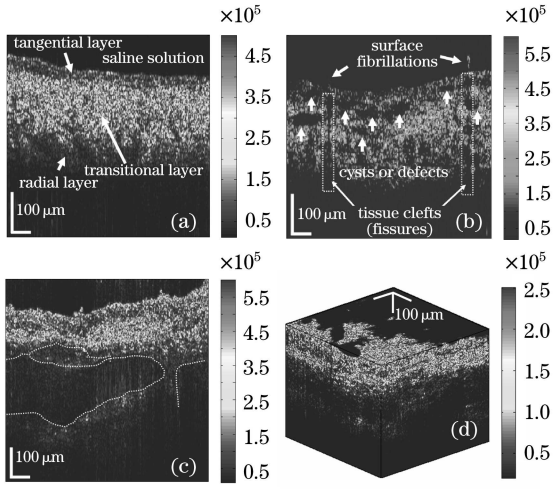

Fig. 3. Image results obtained from chicken knee cartilage: (a) cartilage zones (layers); (b) defects (arrow mark) in cartilage; (c) internal structure layers; (d) 3-D slice and *en face* image.

probe with less reflection at the fiber and saline interface.

The resultant scanned tomograms are shown in Fig. 3, where the image sizes are 1000 (width) × 490 (height) (μm) for (a) and (b), 1000 (width) × 650 (height) (μm) for (c), and 500 (length) × 500 (width) × 540 (height) (μm) for (d). In Fig. 3(a), we can clearly differentiate the characteristic layers of the articular cartilage, which contains the superficial zone (or tangential layer), the middle zone (or transitional layer), and the deep zone (or radial layer) in the axial direction. The middle zone image appears brighter in OCT, due to the lateral distribution of the collagen fibers in that layer, which causes them to be more reflective and gives rise to greater scattering than those in the other two layers having a longitudinal distribution. In addition, because of the reduced index difference ($\Delta n \sim 0.01$) between the saline solution ($\sim$1.34) and tissue surface ($\sim$1.33), more power is able to penetrate into the tissue, which helps to improve the total imaging depth. Also this prevents a strong surface reflection, which would occur in a greater index difference ($\Delta n \sim 0.33$) between the air (1.00) and cartilage surface and thus reduce the overall SNR of the OCT images. Other fundamental limiting factors of the working depth include multiple scattering and the divergence of the beam in the tissue.

In Fig. 3(b), we can clearly observe some of the featured structures in the cartilage, such as defects or cysts, which are marked with arrows. The major fissures in the tissue are marked with dotted rectangles. The width of the cleft and the size of the sac are as small as 5 and 10 μm, respectively. Furthermore, fibrillations of the cartilage, which consist of vertical tears and tangential splits, where the vertical components predominate. These are reported to be caused by either the partial disruption of the surface itself or the detachment of the pre-existing fibrils at the tangential layer, which is one of the forms of collagen disorganization such as surface erosion and thinning caused by cartilage loss[15]. In addition to the vertical surface fibrillations, Fig. 3(c) shows the microstructural information deep in the cartilage marked in white dotted lines in different positions, and a three-dimensional (3D) sliced volume image of the knee cartilage is shown in Fig. 3(d) having a non-even layer structure, as well as an *en face* image at the top surface.

We successfully demonstrated a FD-CPOCT system with a bare fiber probe integrated with a hypodermic needle that can potentially be used for diagnosing diseases related to the articular cartilage. The beam divergence is decreased to a smaller angle and the SNR is improved by the index matched saline solution. We were able to observe very clearly both the pathological structure of the chicken cartilage and the internal and external micro-defects, such as fissures and fibrillations, with finer resolutions than those allowed by other comparable traditional image modalities.

This work was supported by the second stage of the Brain Korea 21 Project in 2009 and a Korean Science and Engineering Foundation (KOSEF) grant funded by the Korea Government (MEST) (No. R01-2008-000-20089-0).

References

1. W. P. Chan, P. Lang, M. P. Stevens, M. S. Sack, E. W. Stoller, C. Basch, and H. K. Genant, Am. J. Roentgenol. **157,** 799 (1991).
2. J. G. Fujimoto, Nature Biotechnol. **21,** 1361 (2003).
3. A. B. Vakhtin, D. J. Kane, W. R. Wood, and K. A. Peterson, Appl. Opt. **42,** 6953 (2003).
4. X. Liu, X. Li, D.-H. Kim, I. Ilev, and J. U. Kang, Chin. Opt. Lett. **6,** 899 (2008).
5. K. M. Tan, M. Mazilu, T. H. Chow, W. M. Lee, K. Taguchi, B. K. Ng, W. Sibbett, C. S. Herrington, C. T. A. Brown, and K. Dholakia, Opt. Express **17,** 2375 (2009).
6. C. R. Chu, D. Lin, J. L. Geisler, C. T. Chu, F. H. Fu, and Y. Pan, Am. J. Sports Med. **32,** 699 (2004).
7. Y. Pan, Z. Li, T. Xie, and C. R. Chu, J. Biomed. Opt. **8,** 648 (2003).
8. C. R. Chu, N. J. Izzo, J. J. Irrgang, M. Ferretti, and R. K. Studer, J. Biomed. Opt. **12,** 051703 (2007).
9. T. Xie, S. Guo, J. Zhang, Z. Chen, and G. M. Peavy, J. Biomed. Opt. **11,** 064001 (2006).
10. X. Li, S. Martin, C. Pitris, R. Ghanta, D. L. Stamper, M. Harman, J. G. Fujimoto, and M. E. Brezinski, Arthritis Res. Ther. **7,** R318 (2005).
11. J.-I. Youn, T. Akkin, and T. E. Milner, Physiol. Meas. **25,** 85 (2004).
12. C. W. Han, C. R. Chu, N. Adachi, A. Usas, F. H. Fu, J. Huard, and Y. Pan, Osteoarthritis Cartilage **11,** 111 (2003).
13. R. Leitgeb, C. K. Hitzenberger, and A. F. Fercher, Opt. Express **11,** 889 (2003).
14. A. M. Rollins and J. A. Izatt, Opt. Lett. **24,** 1484 (1999).
15. G. P. Grieve, *Common Vertebral Joint Problems* (Churchill Livingstone, London, 1988).